

Cite this: *Chem. Sci.*, 2025, **16**, 20968

All publication charges for this article have been paid for by the Royal Society of Chemistry

## Macrocyclic formation-mediated augmentation in reactive oxygen species production

Ao Liu,<sup>a</sup> Youtao Xin,<sup>b</sup> Yong-Kang Zhu,<sup>a</sup> Yuan-Hang Jin,<sup>a</sup> Yue Yang,<sup>a</sup> Hongzhu Chen,<sup>a</sup> Meng-Hao Li,<sup>a</sup> Xin-Yue Lou,<sup>a</sup> Xin Wang,<sup>\*ac</sup> Hui Gao<sup>\*b</sup> and Ying-Wei Yang  <sup>\*a</sup>

While the synthesis of methylene-bridged fluorescent macrocycles has attracted significant research interest, their ability to generate reactive oxygen species (ROS) remains relatively unexplored. Herein, we present a strategy for constructing multifunctional macrocycles through backbone functionalization and successfully synthesize a new class of [2]terphenyl-extended pillar[6]arenes. Upon incorporating benzothiadiazole, highly fluorescent macrocycles with aggregation-induced emission enhancement characteristics, *i.e.*, [2]terphenyl-benzothiadiazole-extended pillar[6]arenes, were obtained. Subsequent studies on modulating side-chain modifications have revealed distinct singlet oxygen ( ${}^1\text{O}_2$ ) generation capabilities. Notably, quaternary ammonium-functionalized macrocycles show lower quantum yields yet superior  ${}^1\text{O}_2$  generation efficiency under light irradiation compared to their ethoxy-modified counterparts and the acyclic building block, while retaining targeted fluorescence imaging capabilities. Significantly, the supramolecular synergy between photodynamic action and ceftizoxime sodium drug complexation drastically enhances antibacterial efficacy compared to individual modalities. This study highlights the potential of quaternary ammonium-functionalized fluorescent macrocycles in  ${}^1\text{O}_2$  generation and offers promising new avenues for developing antibacterial drugs for biomedical applications.

Received 28th August 2025

Accepted 3rd October 2025

DOI: 10.1039/d5sc06637a

[rsc.li/chemical-science](http://rsc.li/chemical-science)

## Introduction

The rapid advancement of supramolecular chemistry is closely linked to the design of macrocyclic compounds with diverse functional and structural attributes. Molecules exhibiting aggregation-induced emission enhancement (AIEE) properties hold considerable promise in bioimaging and the generation of reactive oxygen species (ROS) due to their unique photophysical characteristics.<sup>1,2</sup> Integrating AIEE moieties into macrocyclic compounds with specific functions to achieve functional synergy has become a new strategy for designing and synthesizing novel macrocycles.<sup>3–5</sup> These compounds with inherent structural features are capable of engaging in selective host–guest interactions and have aroused significant interest for their critical roles in diverse fields, including molecular recognition,<sup>6,7</sup> supramolecular self-assembly,<sup>8,9</sup> fluorescent systems,<sup>3,10,11</sup> biological imaging,<sup>12–14</sup> and smart materials.<sup>15–19</sup>

Recently, pillararenes have emerged as a powerful tool in supramolecular chemistry due to their rigid cavity structures, facile synthesis, superb post-modification capabilities, and

excellent host–guest properties.<sup>17,20–25</sup> However, conventional functionalization strategies and fluorescent group incorporation for these systems are predominantly limited to side-chain modifications, constrained by the availability of synthetic precursors. Recent advances in backbone engineering have expanded the structural diversity of pillararene derivatives, include but are not limited to leaning pillar[6]arenes,<sup>26–28</sup> [2] biphenyl-extended pillar[6]arenes,<sup>29–31</sup> azo-macrocycles,<sup>32,33</sup> wreatharene,<sup>34</sup> diimide-extended pillar[6]arene,<sup>35</sup> triphenylamine[3]arenes,<sup>36</sup> tetraphenylethylene[3]arene,<sup>37</sup> and others.<sup>38–41</sup> The synthesis of these macrocycles frequently necessitates specific reaction pathways (Fig. 1a), which complicates the development of a universal synthetic strategy for constructing pillararene-inspired fluorescent macrocycles.

Despite significant progress in the research of fluorescent macrocycles, several challenges remain to be addressed. The primary reason is that the complexity of molecular construction limits the structural diversity of fluorescent macrocyclic systems. There is a relative scarcity of reported pillararene-inspired fluorescent macrocycles, primarily due to the dual challenges presented by their unique molecular topological structure to synthetic chemistry: (a) the  $\pi$ -conjugated system needs to be precisely regulated to achieve the fluorescence emission function; (b) the reasonable arrangement of pre-organized sites has to be considered when constructing the macrocyclic cavity. This multidimensional characteristic of

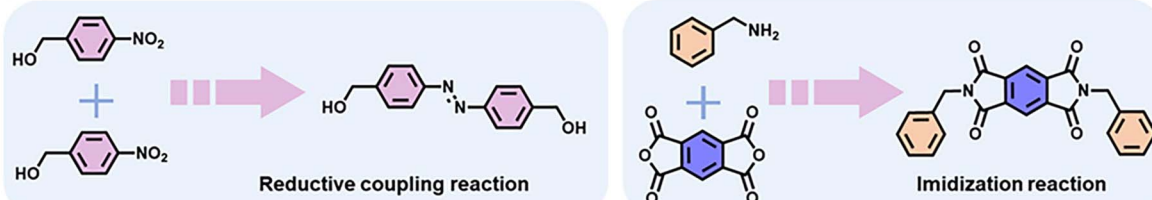
<sup>a</sup>College of Chemistry, Jilin University, 2699 Qianjin Street, Changchun 130012, P. R. China. E-mail: [ywyang@jlu.edu.cn](mailto:ywyang@jlu.edu.cn)

<sup>b</sup>School of Materials Science and Engineering, Tiangong University, Tianjin 300387, P. R. China. E-mail: [huigao@tiangong.edu.cn](mailto:huigao@tiangong.edu.cn)

<sup>c</sup>Department of Radiation Oncology, China-Japan Union Hospital of Jilin University, Changchun 130033, P. R. China. E-mail: [xinwangjlu@jlu.edu.cn](mailto:xinwangjlu@jlu.edu.cn)



## (a) Previous work



## (b) This work

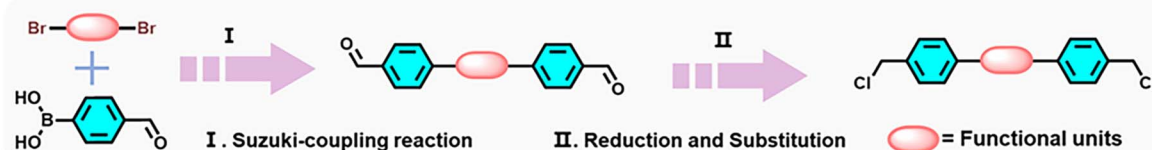
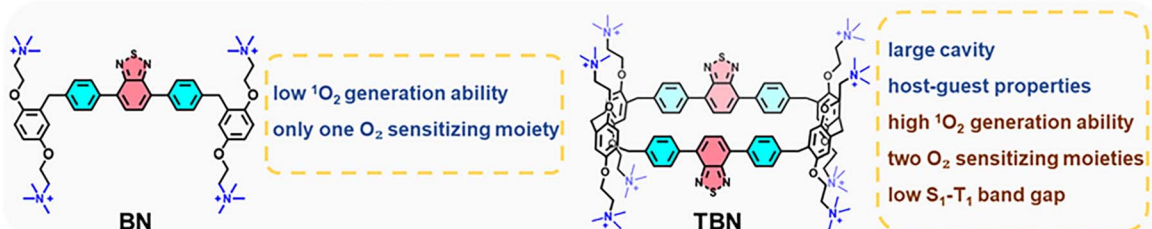
(c) Comparison of the  $^1\text{O}_2$  generation capabilities

Fig. 1 (a) Construction of the pillararene-inspired macrocycles in the previous work. (b) The design of [2]terphenyl-extended pillar[6]arenes ([2]Tp-ExP6) and [2]terphenyl-benzothiadiazole-extended pillar[6]arenes ([2]TpB-ExP6) in this work. (c) Comparison of the  $^1\text{O}_2$  generation ability between the acyclic building block and macrocycle.

structure and function requires precise molecular design to make a delicate balance between spatial conformation, non-covalent intramolecular interactions (such as  $\pi$ - $\pi$  stacking and hydrogen bonding), and electronic properties. In this work, we propose a general synthetic approach that facilitates the introduction of diverse functional entities into the macrocyclic backbone, thereby endowing the synthetic macrocycles with various functional characteristics and unique properties (Fig. 1b).

On the other hand, the preparation of ROS-generating materials and the efficient generation of  $^1\text{O}_2$  in specific environments have garnered extensive attention.<sup>42–45</sup> Certain macrocycles and their derivatives have been studied for ROS generation.<sup>43,44,46–50</sup> However, research in this critical area remains limited due to the challenges in designing and synthesizing macrocycles with specific luminescent properties and ROS-generating capabilities and many scientific problems need to be addressed. Benzothiadiazole, known for its excellent photothermal stability and relatively low energy level of the lowest unoccupied molecular orbital (LUMO), is commonly employed as an electron acceptor covalently linked to electron donors to construct luminescent molecules.<sup>51</sup> Those interesting examples where benzothiadiazole is modified within synthetic macrocycles suggested its great potential.<sup>52–54</sup>

Inspired by the differences in molecular properties resulting from structural changes caused by cyclization reactions, we present a versatile synthetic strategy that enables the modular construction of macrocycles with diverse functionalization.

This strategy capitalizes on the pre-functionalization of dialdehyde precursors with diverse motifs, allowing controlled integration of targeted functional units into the macrocyclic architecture through subsequent cyclization processes. By strategically incorporating terphenyl and benzothiadiazole entities into the dialdehyde building blocks, we obtain two kinds of new macrocycles: [2]terphenyl-extended pillar[6]arenes ([2]Tp-ExP6) and [2]terphenyl-benzothiadiazole-extended pillar[6]arenes ([2]TpB-ExP6) (Fig. 1b). These compounds exhibit specific characteristics, such as easy modification, a rigid backbone, and AIEE properties. To improve the ability to generate  $^1\text{O}_2$ , we then make the ammonium macrocycle TBN, which can change the transition path of photons upon illumination, thereby facilitating the generation of  $^1\text{O}_2$  (Fig. 1c). The water-soluble macrocycle TBN not only exhibits the ability to generate  $^1\text{O}_2$  but also proves excellent synergistic antibacterial activity when combined with ceftizoxime sodium (CZX) and bioimaging. Due to its exceptional photophysical properties, this macrocycle exhibits significant potential as a bacterial imaging agent for labeling bacteria. By integrating photosensitizers with the macrocycle, we can achieve both photodynamic therapy and synergistic antibacterial effects with the drug.

## Results and discussion

### Molecular design and synthesis

The synthetic approach that produced the newly synthesized macrocycles presented in this work is regarded as an essential



and innovative method, which allows for the introduction of different functional groups onto the macrocyclic backbone and, meanwhile, provides a versatile means of structural modification while maintaining the integrity of the core framework (Fig. 1b). Taking **TET** as an illustrative example, the first step involved the synthesis of dialdehyde compound **1** through Suzuki-coupling between 1,4-dibromobenzene and (4-formylphenyl) boronic acid, followed by reduction with  $\text{NaBH}_4$  to quantitatively convert the aldehyde group into benzyl alcohol (Fig. 2a). Subsequently,  $\text{SOCl}_2$  was used as a reagent to convert the hydroxymethyl groups into chloromethyl groups to form compound **2**. The acyclic building block **M-E** was synthesized through a Friedel–Crafts alkylation, wherein compound **2** was reacted with an excess of 1,4-diethoxybenzene in the presence of  $\text{AlCl}_3$  as a catalyst to afford the product in a yield of 40%. After that, a conventional one-pot macrocyclization reaction was conducted using  $\text{BF}_3\text{-Et}_2\text{O}$  as a catalyst, with paraformaldehyde and **M-E** as reactants, yielding **TET** in a 38% yield. The synthetic routes to **TMe**, **TBMe**, and **TBet** followed the same strategy as that of **TET**, demonstrating the versatility of the method in accommodating different subunits. We also synthesized **MBr** using 1,4-bis(2-bromoethoxy)benzene units. The corresponding water-soluble quaternary ammonium compound **BN** was obtained by post-synthetic modification (Fig. 2b). Alternatively,

**MBr** can first undergo cyclization *via* a Friedel–Crafts reaction to yield **TBBr**, which is then further modified using the same post-modification method to obtain the water-soluble macrocycle **TBN** (Fig. 2c). All these macrocycles, including **TMe**, **TEt**, **TBMe**, **TBet**, and **TBN**, were fully characterized by  $^1\text{H}$  NMR,  $^{13}\text{C}$  NMR, and HRMS spectroscopy (Fig. S1–S42).

### Single-crystal X-ray diffraction of macrocycles

Single crystals suitable for X-ray diffraction were obtained by slowly diffusing isopropyl ether into a dichloromethane solution of **TMe** or **TEt** (Fig. 3a and b). X-ray analysis revealed that the macrocycle **TMe**, with a large cavity of  $10.6\text{ \AA} \times 18.5\text{ \AA}$ , adopts an inclined stacking arrangement, with a molecular packing pattern resembling the leaning pillar[6]arene (LP6).<sup>26</sup> This arrangement highlights the macrocycle's large cavity and structural adjustability, and the strategy has proven effective in expanding the effective cavity of the macrocycle. Moreover, the observed packing mode indicates that the stacking structure may possess similar ordering, with distinct spatial symmetry and regularity in arrangement, thereby providing important insights for further exploration of its structural properties. The ethoxy-modified macrocycle **TEt** was synthesized by converting dimethoxybenzene to diethoxybenzene. Remarkably, in the

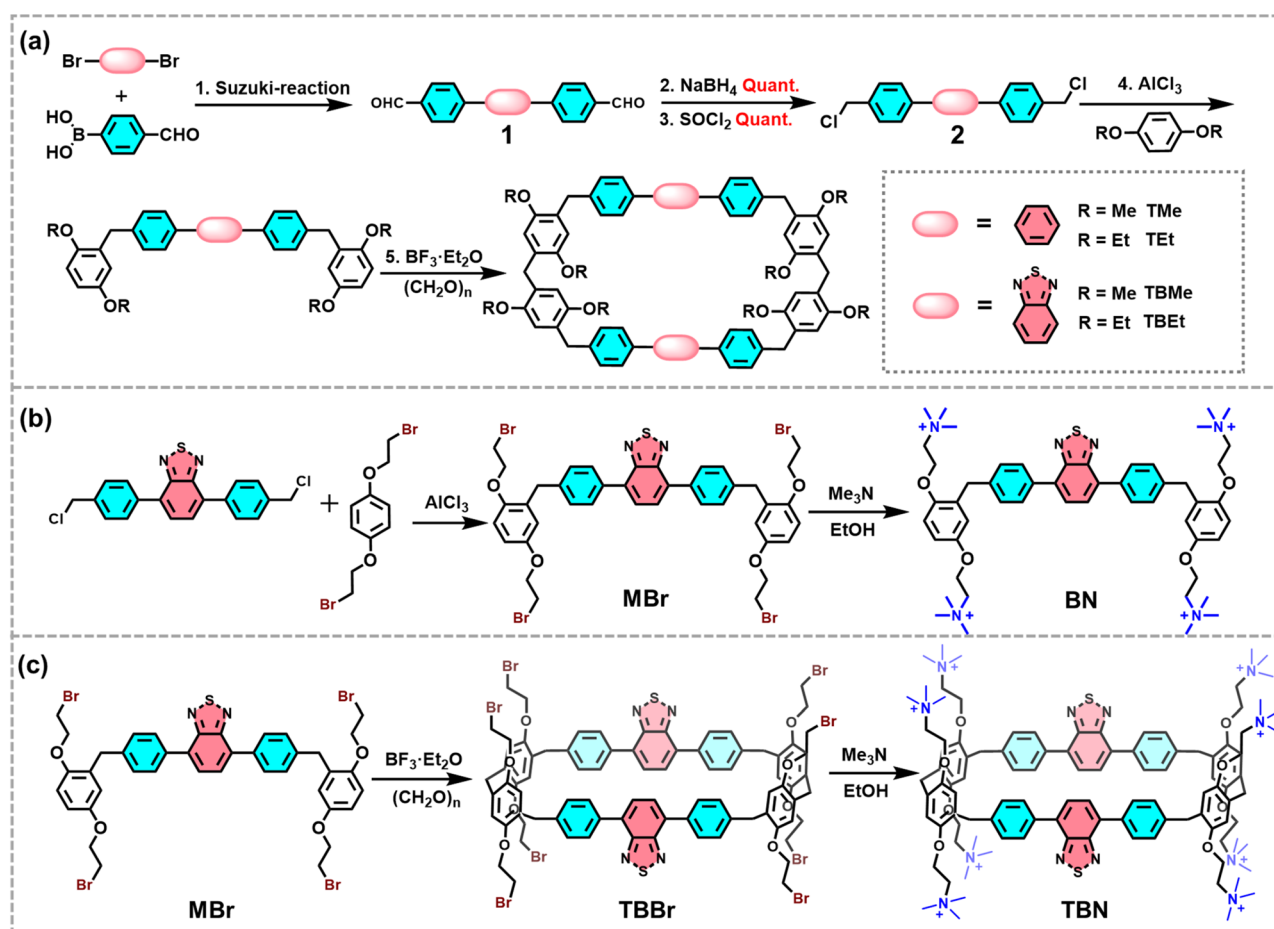


Fig. 2 Synthetic routes to (a) **TMe**, **TEt**, **TBMe**, and **TBet**, (b) **BN**, and (c) **TBN**.



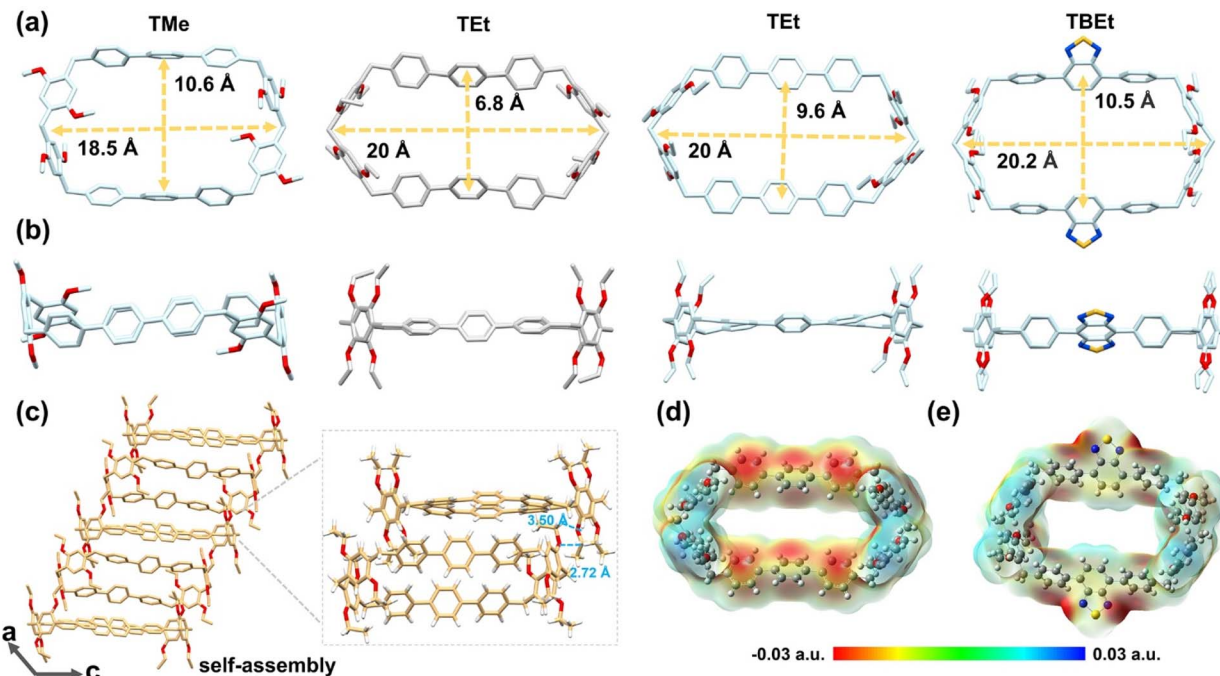


Fig. 3 (a and b) Crystal structure of TMMe, TEt, and TBEt from top view and side view. (c) The packing mode of TEt viewed along the [010] direction highlights the self-assembly by C–H...O interaction of the macrocycle. Electric potential of (d) TEt and (e) TBEt.

solid state, TEt exhibits a unique structural feature, adopting two distinct conformations within a single unit cell, with cavity dimensions of  $6.8 \text{ \AA} \times 20 \text{ \AA}$  and  $9.6 \text{ \AA} \times 20 \text{ \AA}$ . The spatial arrangement of the molecule results in different geometric orientations, with the angles formed between the central and peripheral benzene planes being  $61.3^\circ$  and  $82.2^\circ$ , respectively (Fig. S43). This distinctive conformational flexibility is a notable aspect of the molecular structure, which might contribute to its functional properties or interactions in the solid state. Viewed along the  $\alpha$ -axis, the two macrocycles of TEt in the packing state do not overlap; instead, they adopt an alternating stacking arrangement. This unique arrangement indicates a well-organized, non-overlapping packing pattern that contributes to the stability and integrity of the crystalline structure. They are assembled through the C–H...O interaction involving the side chain of TEt (Fig. 3c). The packing arrangement of both crystal types reveals leaning structures similar to those observed in LP6 (ref. 26) and [2]biphenyl-extended pillar[6]arene ([2]Bp-ExP6).<sup>29</sup> To further investigate the crystal morphology, scanning electron microscopy (SEM) images were obtained, which provide a high-resolution view of the crystalline surface. These images show that the morphology of the crystals closely matches the bulk crystal appearance of TEt, exhibiting a distinct cuboid shape (Fig. S44).

A single-crystal of TBEt suitable for X-ray diffraction was obtained by slowly diffusing its 1,4-dioxane solution at room temperature for 2 days. In the solid state, TBEt exhibits a hexagonal structure with dimensions of  $10.4 \text{ \AA} \times 20 \text{ \AA} \times 10 \text{ \AA}$ , where the two benzothiadiazole groups are oriented in opposite directions (Fig. 3a and b). Solvent molecules of 1,4-dioxane sequentially occupy the intermolecular void, bridging adjacent

TBEt units through C–H...O interactions. The macrocycle maintains an inclined stacking mode, further corroborating the structural consistency observed within this class of macrocycles. Similar to TEt, TBEt undergoes self-assembly driven by side-chain interactions, as confirmed by its crystal structure (Fig. S45). What's more, the geometry of H between the ethoxy groups was further validated through 2D ROESY experiments in  $\text{CDCl}_3$  (Fig. S46 and S47), which confirmed significant spatial proximity and interaction between the side chains in solution. These findings provide compelling evidence of the robust structural and interactional paradigms governing this new family of macrocycles.

### Photophysical properties

In TBEt, the benzothiadiazole unit acts as an electron-deficient group, forming a classic donor–acceptor–donor (D–A–D) structure with the adjacent benzene rings. Compared with TEt, the benzothiadiazole region of TBEt is more electronegative (Fig. 3d and e). The introduction of benzothiadiazole into [2]Tp-ExP6 induces a significant red shift in fluorescence, with the emission shifting from 357 nm in [2]Tp-ExP6 to 506 nm in [2]TpB-ExP6 (Fig. S48–S50). The Stokes shift increased significantly from 70 nm in TET to 220 nm in TBEt (Fig. 4a and b). Notably, the post-modified TBMe maintained this enhanced Stokes shift characteristic. Based on the advantageous properties demonstrated by the [2]TpB-ExP6 macrocycles, we conducted a more in-depth investigation into their photophysical characteristics. As illustrated in Fig. S51, both TBMe and TBEt exhibit significantly enhanced fluorescence emission in  $\text{CHCl}_3$  compared to their respective acyclic building blocks, a phenomenon commonly observed following macrocyclization.



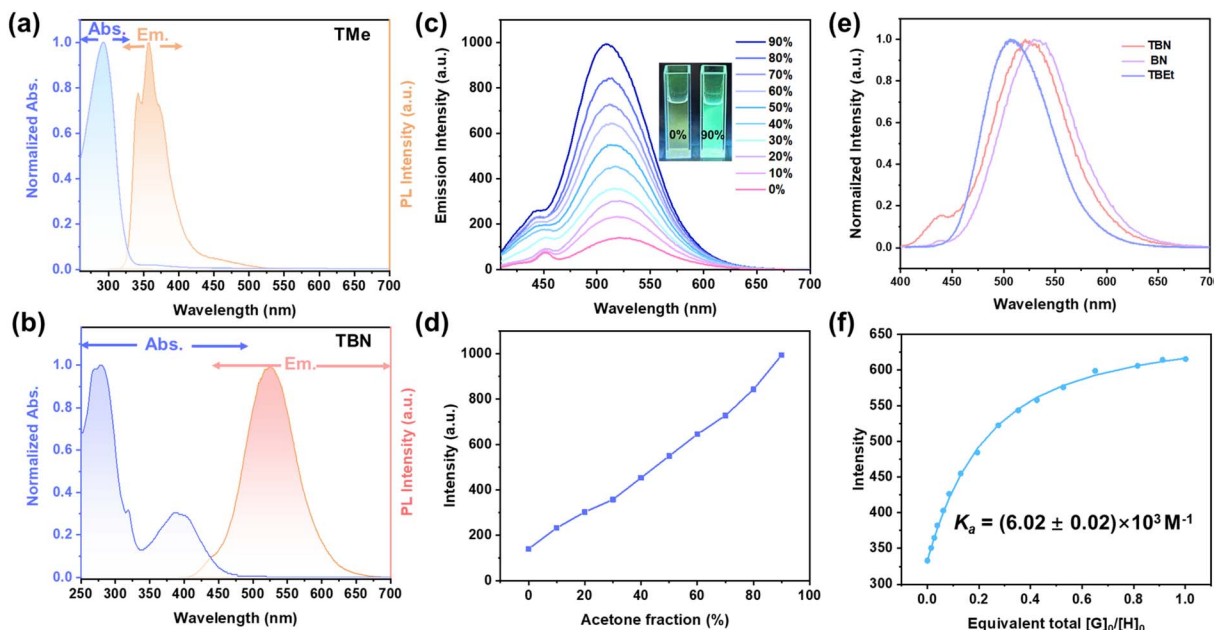


Fig. 4 (a) UV-vis absorption spectrum and fluorescence spectrum of **TMe** in CHCl<sub>3</sub>. (b) UV-vis absorption spectrum and fluorescence spectrum of **TBN** in H<sub>2</sub>O. (c and d) AIE properties of **TBN** in H<sub>2</sub>O/Acetone. (e) Fluorescence spectrum of **TBN**, **BN**, and **TBET**. (f) Host–guest association constants of **TBN** and **CZX**.

However, the fluorescence emission of these macrocycles remains relatively insensitive to changes in solvent polarity. Using **TBET** as an example, its fluorescence emission was analyzed in mixed DMF/water systems. The emission intensity of **TBET** increased proportionally with the addition of water, a poor solvent for the compound (Fig. S52). A Tyndall effect, performed in 80% water with a pronounced light scattering path, indicated aggregate formation. Complementary SEM analyses under varying water contents revealed a distinct morphological transition: at low aggregation levels, the material existed as discrete entities with relatively large dimensions, whereas progressive aggregation resulted in a more compact spatial arrangement accompanied by a marked reduction in particle size (Fig. S53). Similar fluorescence enhancement was also observed in acetone/water mixtures, further demonstrating the AIEE effect. This is strongly indicative of the AIEE properties of the macrocycle. Additionally, the acyclic building block **BN-E** and the macrocycle **TBET** exhibited fluorescence emissions in blue and green, respectively, with peak wavelengths at approximately 488 and 507 nm in the solid states, showing a significant red shift in their emission spectra in the solid state. Fluorescence lifetime and quantum efficiency of the macrocycles and acyclic building blocks modified with benzothiadiazole were measured (Fig. S54–S60). Notably, the macrocycle **TBET** exhibited a red shift in its emission spectrum and still maintained a high quantum yield of 61%, compared to **BN-E**'s quantum yield of 52%. Similarly, **BN** and the macrocycle **TBMe** exhibited comparable photophysical properties. This result underscores the photophysical stability of macrocyclization, further validating the potential of benzothiadiazole-modified macrocycles for advanced photophysical applications.

### Evaluation of ROS generation ability

We explored the synthesis of a water-soluble macrocycle and evaluated its ROS production capabilities. The fluorescence emission of the water-soluble **TBN** was observed at 526 nm, exhibiting a 20 nm red shift compared to that (506 nm) of **TBET** and similar to the acyclic building block **BN** (Fig. 4e). Further investigation of its fluorescence behavior in a water/acetone system (Fig. 4c and d) revealed that as the acetone content (a poor solvent) increased, the fluorescence intensity was enhanced. This result confirms that the macrocycle retained its AIEE properties even after water solubilization. Additionally, in the solid state, **TBN** exhibited a quantum yield of 13% and a fluorescence lifetime of 4.16 ns (Fig. S56).

We then chose 9,10-anthracenediyl-bis(methylene) dimalonic acid (ABDA) as the probe to detect the production capacities of  ${}^1\text{O}_2$  under the illumination of white light. The absorbance of ABDA decreased over time in the presence of **TBN** as the generation of  ${}^1\text{O}_2$  induced a [4 + 2] cycloaddition of the anthracene moiety in ABDA, forming an endoperoxide at the central ring, while the absorbance of ABDA (blank control) was hardly changed (Fig. 5a and d). Under the same conditions, the absorbance reduction in the presence of **BN** was less than 20%, indicating that **TBN** exhibits significantly stronger  ${}^1\text{O}_2$  generation ability than **BN** (Fig. 5b and S61). **TBET** cannot generate  ${}^1\text{O}_2$  (Fig. S62). We also use dichlorodihydrofluorescein (DCFH) as the probe to detect the production capacities of ROS (Fig. S63). What's more, the host–guest complex remains excellent  ${}^1\text{O}_2$  generation ability (Fig. 5c). To further compare the antibacterial advantages of the macrocycle with the acyclic building block, we measured their zeta potentials (Fig. 5f). The macrocycle is more positively charged, making it easier to adsorb onto the

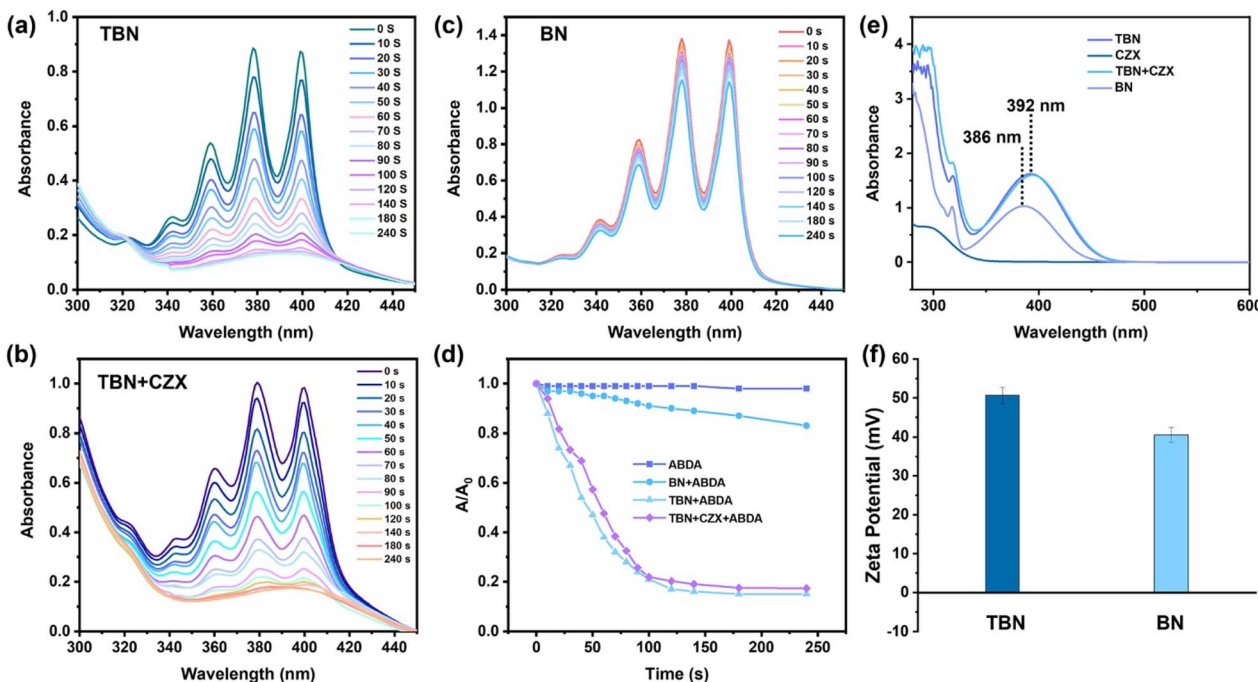


Fig. 5 UV-vis absorption of (a) TBN, (b) TBN+CZX, and (c) BN in PBS (pH = 7.4) under white light irradiation (20 W) with ABDA as an indicator. (d)  $^1\text{O}_2$  productivity of BN, TBN, and TBN+CZX in PBS (pH = 7.4) under white light irradiation (20 W) with ABDA as an indicator. (e) UV-vis absorption of TBN, TBN+CZX, BN, and CZX in PBS (pH = 7.4,  $c = 10^{-4}$  M). (f) Zeta potential of TBN and BN.

negatively charged bacterial cell membrane through electrostatic interactions, should its use as an antibiotic be considered.

To elucidate the enhanced ROS generation capability of macrocycles compared to the acyclic building block, we first performed geometric optimization on the macrocyclic compound **TBN** and its acyclic building block **BN** (Fig. 6a). Subsequently, the energies of the frontier molecular orbitals (HOMO and LUMO) for both species were calculated (Fig. 6b). The computational results reveal that **TBN** exhibits a LUMO energy level of  $-13.32$  eV and a HOMO energy level of  $-16.49$  eV, corresponding to a HOMO-LUMO gap ( $\Delta E$ ) of  $3.17$  eV. In contrast, **BN** shows a LUMO energy of  $-7.33$  eV, a HOMO energy of  $-10.71$  eV, and a gap of  $3.38$  eV. Corresponding to their UV absorption, the absorption peak of the macrocycle is at  $392$  nm and that of the acyclic building block is at  $386$  nm (Fig. 5e). The observed electronic structure strongly corroborates the significant performance enhancement achieved through macrocyclization. Collectively, these computational findings indicate that the macrocyclic structure facilitates a reduction in the molecular excitation energy, rendering its electrons more readily excitable. Based on the energy level diagrams, it is evident that **TBN** exhibits a superior capability for  $^1\text{O}_2$  generation compared to **BN** (Fig. 6c and d). This advantage stems from the smaller energy gap between the singlet and triplet states ( $\Delta E_{S_1-T_1}$ ) in **TBN** ( $0.86$  eV), compared to **BN** ( $1.04$  eV), which is a critical factor indicating more efficient intersystem crossing – the key process required for  $^1\text{O}_2$  formation. Therefore, the combination of these factors clearly demonstrates that **TBN** is more effective at generating  $^1\text{O}_2$  than **BN**.

### Photodynamic antibacterial performance

Based on the photophysical properties of **TBN**, flow cytometry experiments (Fig. 7a and b) were conducted to validate its targeting capability for *Escherichia coli* (*E. coli*) and *Staphylococcus aureus* (*S. aureus*). The control group (orange peak) exhibits low fluorescence intensity, while the experimental group (blue peak) shows a significant shift towards higher fluorescence intensity. This distinct separation between the two peaks indicates that **TBN** effectively binds to *E. coli* and *S. aureus*, confirming its strong targeting ability under experimental conditions. After co-incubating two types of bacteria with **TBN**, bacterial imaging experiments were performed using a confocal laser scanning microscope (CLSM), as shown in Fig. 7c. Both bacterial strains exhibited bright green fluorescence, confirming the effective interaction and internalization of **TBN** within the bacteria. These results provide strong evidence that the quaternary ammonium groups in **TBN** facilitate bacterial binding, laying the groundwork for further antimicrobial studies. To address the limited efficacy of **CZX**, a third-generation cephalosporin, against Gram-positive *S. aureus* and methicillin-resistant *Staphylococcus aureus* (MRSA), we developed a mixed system using the **TBN** macrocycle. This system leverages the complementary properties of **CZX** that are effective against Gram-negative *E. coli* but less potent against Gram-positive bacteria and the macrocycle's unique bactericidal capabilities, including its  $^1\text{O}_2$  generation, to enhance broad-spectrum antibacterial activity. The  $1:1$  binding stoichiometry between **TBN** and **CZX** was confirmed through multiple spectroscopic techniques.  $^1\text{H}$  NMR studies in  $\text{D}_2\text{O}$  (Fig. S64) revealed upfield shifts in **CZX**

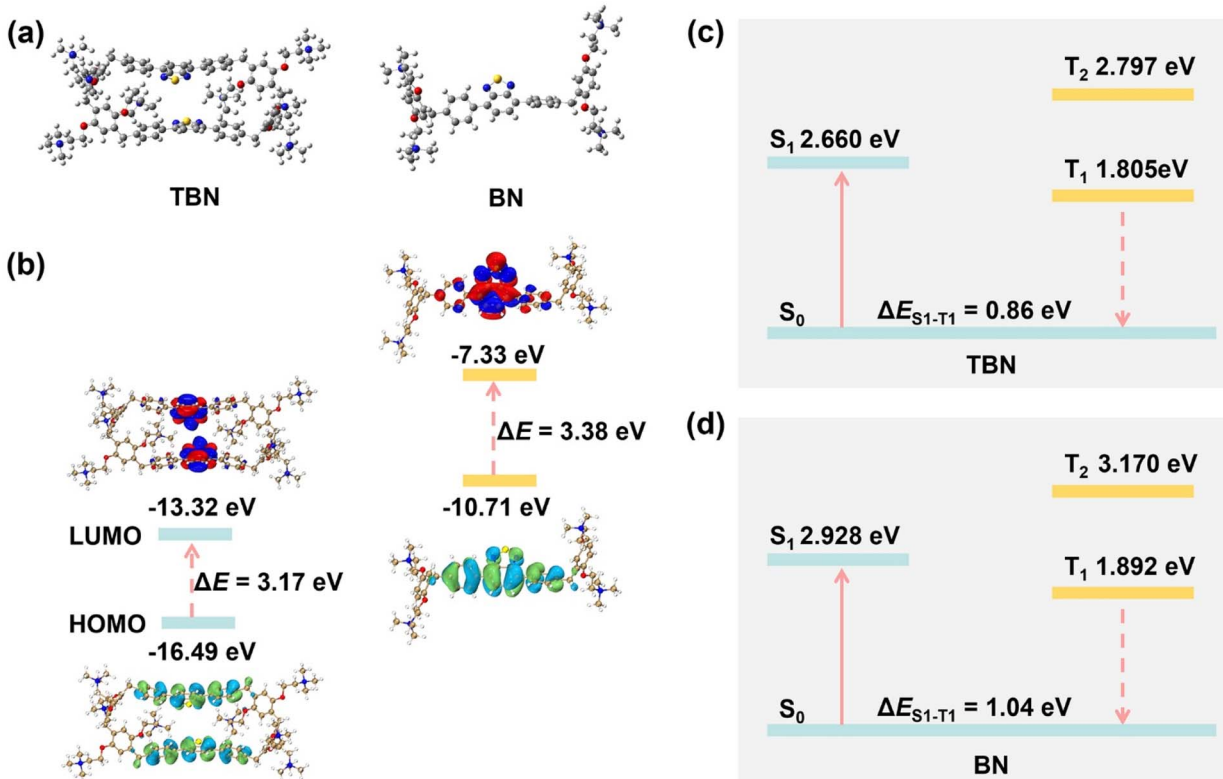


Fig. 6 (a) Simulated structures and (b) molecular orbitals of TBN and BN. Energy-level diagram of ground and excited states of (c) TBN and (d) BN.

protons upon complexation, indicating an inclusion-induced shielding effect. Job plot analysis by fluorescence spectral further validated the 1:1 binding ratio. HRMS spectrum also confirmed the formation of the complex (Fig. S65). Fluorescence

titration and isothermal titration calorimetry (Fig. 4f and S66–S68) yielded an association constant ( $K_a = (6.02 \pm 0.02) \times 10^3 \text{ M}^{-1}$ ), demonstrating good host–guest affinity. A simulated host–guest complex structure was obtained (Fig. S69).

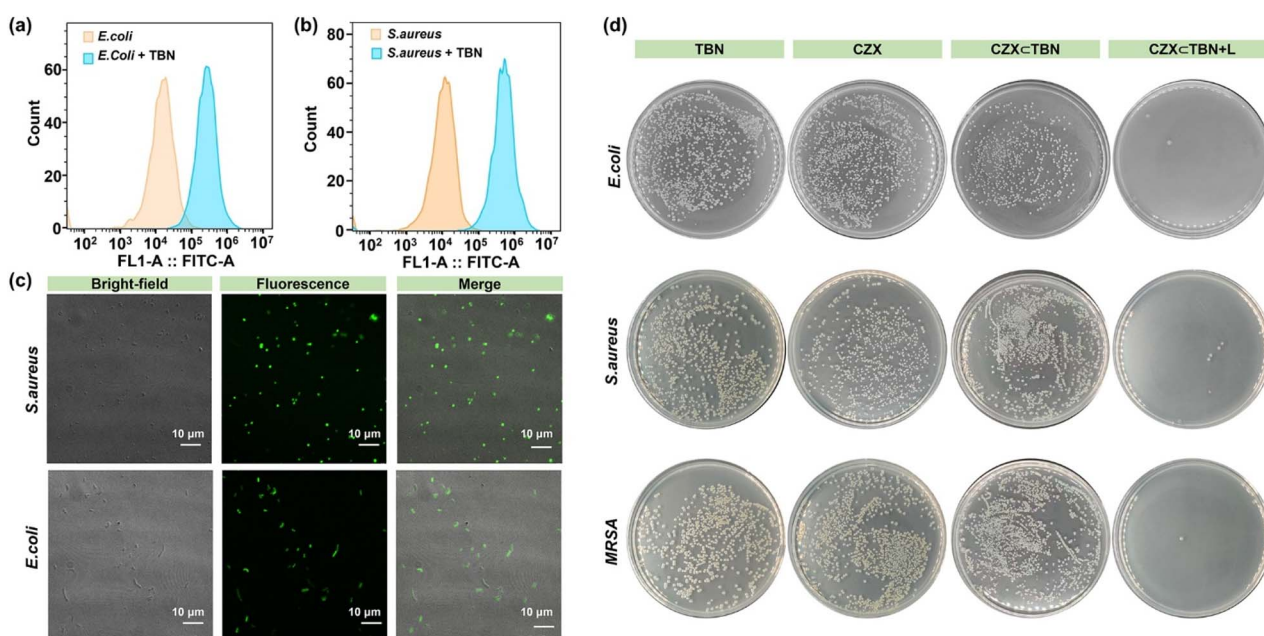


Fig. 7 Flow cytometry experiments of (a) *E. coli* and (b) *S. aureus* after incubation with TBN. (c) CLSM images of *E. coli* and *S. aureus* treated with TBN. Scale bar: 10  $\mu\text{m}$ . (d) The photos of colony-forming units of *E. coli*, *S. aureus*, and MRSA after being treated with TBN, CZX, and the TBN/CZX complex under both light and dark conditions.

To assess the contribution of host-guest binding to antibacterial activity, anthraquinone-2,6-disulfonic acid disodium salt, with stronger affinity to **TBN** than **CZX**, was used as a competitive guest (G1, Fig. S70–S72). The maximum inhibitory concentration (MIC) experiments of the macrocycle **TBN**, guests **CZX**, and **G1** (MIC >1000  $\mu\text{M}$ ) were subsequently determined (Fig. S73–S77). In *S. aureus*, competitive guests released **CZX**, enabling **TBN** and **CZX** to act independently with slightly reduced antibacterial effect than the host-guest complex (Fig. S78).

After validating the host-guest interactions in standalone antibacterial assays, light irradiation was introduced as an additional factor to enhance antibacterial efficacy and reduce the required drug dosage. By combining **CZX**'s intrinsic activity with bacterial targeting of **TBN** and  $^1\text{O}_2$ -mediated bactericidal effects, the system overcomes the limitations of **CZX** mono-therapy. The **TBN/CZX** complex demonstrated significantly enhanced antibacterial activity under white light compared to dark conditions, as evidenced by MIC experiments and the cell colonies (Fig. 7d and S79–S81). Against *E. coli*, MIC values decreased from 6.25  $\mu\text{M}$  (dark) to 1.5  $\mu\text{M}$  (light), while *S. aureus* and MRSA showed reductions from 250 to 31.25  $\mu\text{M}$  (Fig. S82–S84). This light-activated enhancement correlates with  $^1\text{O}_2$  generation, as confirmed by the macrocycle's superior  $^1\text{O}_2$  production compared to **BN**. Notably, the system exhibited greater potency against Gram-negative *E. coli* than Gram-positive *S. aureus*, with minimal biofilm eradication concentration (MBEC) values of 1.5  $\mu\text{M}$  for *E. coli* versus 62.5  $\mu\text{M}$  for both *S. aureus* and MRSA (Fig. S85). SEM morphological analysis revealed substantial bacterial membrane damage in treated groups (Fig. S86–S88), demonstrating a dual mechanism: biofilm disruption *via* quaternary ammonium groups and  $^1\text{O}_2$ -mediated cellular destruction. Control experiments confirmed minimal antibacterial activity for **TBN** alone under dark conditions, while light-exposed macrocycles showed moderate bactericidal effects attributable to  $^1\text{O}_2$  generation. These results demonstrate that the synergistic effects of the complex as a promising light-responsive antimicrobial platform combining physical biofilm disruption and photodynamic therapy mechanisms.

The cytotoxicity of **TBN** was evaluated on mammalian cells (L929) at various concentrations ranging from 0 to 250  $\mu\text{M}$  (Fig. S89). The results indicate that the cell viability remained above 90% at all tested concentrations, demonstrating low cytotoxicity and excellent biocompatibility. The hemolytic activity of **TBN** was evaluated using sheep red blood cells in the presence of PBS as a negative control, Triton X-100 (1%) as a positive control, and varying concentrations of the complex under non-irradiated conditions. As shown in Fig. S90, **TBN** exhibited negligible hemolytic activity across all tested concentrations, with hemolysis rates remaining below 5%. In contrast, Triton X-100 caused nearly 100% hemolysis, validating its use as a positive control. These results indicate that **TBN** demonstrates excellent hemocompatibility, supporting its safety for further biological and antibacterial applications.

## Conclusions

In summary, we designed and synthesized a new class of [2]Tp-ExP6 macrocycles, achieving precise backbone functionalization that broadened the design flexibility of supramolecular systems. Structural characterization revealed that these expanded macrocycles exhibit the characteristic leaning stacking arrangement while offering superior functional adaptability. Notably, the D-A-D structured [2]TpB-ExP6 exhibited enhanced photophysical properties, with systematic side-chain engineering unveiling a critical structure–function relationship: quaternary ammonium modification induced a trade-off between reduced quantum efficiency and substantially improved  $^1\text{O}_2$  generation efficiency, enabling effective bacterial-targeted imaging. The macrocycle exhibited synergistic antibacterial performance with **CZX**. Comprehensive antimicrobial evaluations against *E. coli*, *S. aureus*, and MRSA demonstrated that the **TBN/CZX** complex under photoactivation achieved superior bactericidal effects compared to **CZX** alone, effectively overcoming the intrinsic limitations of conventional antibiotic therapy. This work demonstrates a powerful strategy for generating  $^1\text{O}_2$  by modifying the side chain and establishing a multifunctional platform that integrates imaging and antibacterial capabilities through rational macrocycle design. It also highlighted the great potential of synthetic macrocycles in advanced therapeutic systems. The strategy not only opens new avenues for the application of supramolecular macrocycles in photodynamic systems but also provides a feasible approach for developing synergistic antimicrobial materials, offering new perspectives for combating drug-resistant bacterial infections.

## Author contributions

All authors have given approval to the final version of the manuscript.

## Conflicts of interest

The authors declare no competing interests.

## Data availability

CCDC 2424138, 2424139 and 2422100 contain the supplementary crystallographic data for this paper.<sup>55a–c</sup>

The original data supporting this article are available in the main text and supporting information (SI). Supplementary information is available. See DOI: <https://doi.org/10.1039/d5sc06637a>.

## Acknowledgements

The authors acknowledge the National Natural Science Foundation of China (no. 22571119 and 52173200), the Natural Science Foundation of Jilin Province (no. 20230101052JC), and the “Medicine + X” cross-innovation team of Bethune Medical Department of Jilin University “Leading the Charge with Open Competition” construction project (no. 2022JBGS04) for



financial support. This paper is dedicated to the memory of Sir James Fraser Stoddart (1942–2024).

## Notes and references

- Y. Wang, J. Liao, Y. Lyu, Q. Guo, Z. Zhu, X. Wu, J. Yu, Q. Wang and W.-H. Zhu, *Adv. Funct. Mater.*, 2023, **33**, 2301692.
- R. Qu, X. Zhen and X. Jiang, *CCS Chem.*, 2022, **4**, 401–419.
- G. Wu and Y.-W. Yang, *Cell Rep. Phys. Sci.*, 2024, **5**, 101873.
- X.-Y. Lou and Y.-W. Yang, *Aggregate*, 2020, **1**, 19–30.
- X.-N. Han, Y. Han and C.-F. Chen, *Angew. Chem., Int. Ed.*, 2025, **64**, e202424276.
- S. Tashiro and M. Shionoya, *Acc. Chem. Res.*, 2020, **53**, 632–643.
- K. Zhang, X.-Y. Lou, Y. Wang, W. Huan and Y.-W. Yang, *Chin. Chem. Lett.*, 2024, **6**, 110464.
- X.-N. Sun, A. Liu, K. Xu, Z. Zheng, K. Xu, M. Dong, B. Ding, J. Li, Z.-Y. Zhang and C. Li, *Aggregate*, 2024, **5**, e607.
- B. Liang, Y. Cheng, X. Liu, L. Jia, X. Wei, Q. Zheng, P. Wang, D. Xia and X. Yan, *Sci. China Chem.*, 2024, **67**, 3373–3381.
- W.-L. Guan, J.-F. Chen, J. Liu, B. Shi, H. Yao, Y.-M. Zhang, T.-B. Wei and Q. Lin, *Coord. Chem. Rev.*, 2024, **507**, 215717.
- S. Izumi, H. F. Higginbotham, A. Nyga, P. Stachelek, N. Tohnai, P. d. Silva, P. Data, Y. Takeda and S. Minakata, *J. Am. Chem. Soc.*, 2020, **142**, 1482–1491.
- S. Song, H. Zhang and Y. Liu, *Acc. Mater. Res.*, 2024, **5**, 1109–1120.
- Z. Gao, X. Zheng, X. Dong, W. Liu, J. Sha, S. Bian, J. Li, H. Cong, C.-S. Lee and P. Wang, *Adv. Healthcare Mater.*, 2024, **13**, 2401778.
- X.-Y. Lou, K. Zhang, Y. Bai, S. Zhang, Y. Li and Y.-W. Yang, *Angew. Chem., Int. Ed.*, 2025, **64**, e202414611.
- J.-R. Wu and Y.-W. Yang, *Angew. Chem., Int. Ed.*, 2021, **60**, 1690–1701.
- Z. Li and Y.-W. Yang, *Acc. Mater. Res.*, 2021, **2**, 292–305.
- K. Jie, Y. Zhou, E. Li and F. Huang, *Acc. Chem. Res.*, 2018, **51**, 2064–2072.
- J.-R. Wu, G. Wu, D. Li, M.-H. Li, Y. Wang and Y.-W. Yang, *Nat. Commun.*, 2023, **14**, 5954.
- G. Zhang, K. Zhang, X.-Y. Lou, X. Li, C.-L. Song, W. Huan and Y.-W. Yang, *ACS Mater. Lett.*, 2024, **6**, 446–451.
- T. Ogoshi, S. Kanai, S. Fujinami, T.-a. Yamagishi and Y. Nakamoto, *J. Am. Chem. Soc.*, 2008, **130**, 5022–5023.
- D. Cao, Y. Kou, J. Liang, Z. Chen, L. Wang and H. Meier, *Angew. Chem., Int. Ed.*, 2009, **48**, 9721–9723.
- X. Li, M. Shen, J. Yang, L. Liu and Y.-W. Yang, *Adv. Mater.*, 2024, **36**, 2313317.
- T. Ogoshi, T.-a. Yamagishi and Y. Nakamoto, *Chem. Rev.*, 2016, **116**, 7937–8002.
- Z.-Q. Wang, X. Wang and Y.-W. Yang, *Adv. Mater.*, 2024, **36**, 2301721.
- X.-Y. Lou and Y.-W. Yang, *Adv. Mater.*, 2020, **32**, 2003263.
- J.-R. Wu, A. U. Mu, B. Li, C.-Y. Wang, L. Fang and Y.-W. Yang, *Angew. Chem., Int. Ed.*, 2018, **57**, 9853–9858.
- H. Zhang, X. Wang, K.-T. Huang, F. Liang and Y.-W. Yang, *Org. Lett.*, 2021, **23**, 4677–4682.
- J.-R. Wu, B. Li and Y.-W. Yang, *Angew. Chem., Int. Ed.*, 2020, **59**, 2251–2255.
- B. Gao, L.-L. Tan, N. Song, K. Li and Y.-W. Yang, *Chem. Commun.*, 2016, **52**, 5804–5807.
- D. Dai, Z. Li, J. Yang, C. Wang, J.-R. Wu, Y. Wang, D. Zhang and Y.-W. Yang, *J. Am. Chem. Soc.*, 2019, **141**, 4756–4763.
- D. Dai, J. Yang, Y.-C. Zou, J.-R. Wu, L.-L. Tan, Y. Wang, B. Li, T. Lu, B. Wang and Y.-W. Yang, *Angew. Chem., Int. Ed.*, 2021, **60**, 8967–8975.
- Y. Liu, H. Wang, P. Liu, H. Zhu, B. Shi, X. Hong and F. Huang, *Angew. Chem., Int. Ed.*, 2021, **60**, 5766–5770.
- Y. Liu, H. Wang, L. Shangguan, P. Liu, B. Shi, X. Hong and F. Huang, *J. Am. Chem. Soc.*, 2021, **143**, 3081–3085.
- S. Niu, L.-L. Mao, H. Xiao, Y. Zhao, C.-H. Tung, L.-Z. Wu and H. Cong, *Chin. Chem. Lett.*, 2022, **33**, 1970–1974.
- F. Zeng, L. Cheng, G.-C. Ou, L.-L. Tang and M.-H. Ding, *J. Org. Chem.*, 2022, **87**, 3863–3867.
- W. Fang, J. Zhang, M. Guo, Y. Zhao and A. C.-H. Sue, *Angew. Chem., Int. Ed.*, 2024, **63**, e202409120.
- F. Zeng, L.-L. Tang, W.-H. Bao and Y.-Z. Tan, *Org. Chem. Front.*, 2024, **11**, 3404–3408.
- H. Zeng, P. Liu, H. Xing and F. Huang, *Angew. Chem., Int. Ed.*, 2022, **61**, e202115823.
- J. Yang, X.-Y. Lou, D. Dai, J. Shi and Y.-W. Yang, *Chin. Chem. Lett.*, 2025, **36**, 109818.
- Z. Wang, L. Zhao, Z. Zhang, X. Sheng, H. Yue, R. Liu, Z. Liu, Y. Li, L. Shao, Y. L. Peng, B. Hua and F. Huang, *J. Am. Chem. Soc.*, 2025, **147**, 4210–4218.
- D. Li, G. Wu, Y.-K. Zhu and Y.-W. Yang, *Angew. Chem., Int. Ed.*, 2024, **63**, e202411261.
- V.-N. Nguyen, Z. Zhao, B. Z. Tang and J. Yoon, *Chem. Soc. Rev.*, 2022, **51**, 3324–3340.
- X. Zheng, S.-N. Lei, Z. Gao, X. Dong, H. Xiao, W. Liu, C.-H. Tung, L.-Z. Wu, P. Wang and H. Cong, *Chem. Sci.*, 2023, **14**, 3523–3530.
- Y. Xu, W. Tuo, L. Yang, Y. Sun, C. Li, X. Chen, W. Yang, G. Yang, P. J. Stang and Y. Sun, *Angew. Chem., Int. Ed.*, 2022, **61**, e202110048.
- L. Shao, Y. Pan, B. Hua, S. Xu, G. Yu, M. Wang, B. Liu and F. Huang, *Angew. Chem., Int. Ed.*, 2020, **59**, 11779–11783.
- X. Dong, X. Dai, G. Li, Y.-M. Zhang, X. Xu and Y. Liu, *Adv. Sci.*, 2022, **9**, 2201962.
- X. Wang, L. Ma, C. Li and Y.-W. Yang, *Chem. Mater.*, 2024, **36**, 2177–2193.
- S. Gao, X. Yan, G. Xie, M. Zhu, X. Ju, P. J. Stang, Y. Tian and Z. Niu, *Proc. Natl. Acad. Sci. U.S.A.*, 2019, **116**, 23437–23443.
- Y. Yao, R. Zhao, Y. Shi, Y. Cai, J. Chen, S. Sun, W. Zhang and R. Tang, *Chem. Commun.*, 2018, **54**, 8068–8071.
- Z. Lei, Y.-H. Song, Y.-L. Leng, Y.-J. Gu, M. Yu, Y. Chen, Q. Yu and Y. Liu, *J. Med. Chem.*, 2025, **68**, 5891–5906.
- H. Gu, W. Liu, H. Li, W. Sun, J. Du, J. Fan and X. Peng, *Coord. Chem. Rev.*, 2022, **473**, 214803.



52 Z.-L. Qiu, C. Tang, X.-R. Wang, Y.-Y. Ju, K.-S. Chu, Z.-Y. Deng, H. Hou, Y.-M. Liu and Y.-Z. Tan, *Angew. Chem., Int. Ed.*, 2020, **59**, 20868–20872.

53 S. Li, K. Liu, X.-C. Feng, Z.-X. Li, Z.-Y. Zhang, B. Wang, M. Li, Y.-L. Bai, L. Cui and C. Li, *Nat. Commun.*, 2022, **13**, 2850.

54 S. Li, Q. Liu, L. Mao, X. Zhang, C. Li and D. Ma, *Chin. Chem. Lett.*, 2024, **35**, 109791.

55 (a) CCDC 2424138, Experimental Crystal Structure Determination, 2025, DOI: [10.5517/ccdc.csd.cc2mcj0k](https://doi.org/10.5517/ccdc.csd.cc2mcj0k); (b) CCDC 2424139, Experimental Crystal Structure Determination, 2025, DOI: [10.5517/ccdc.csd.cc2mcj1l](https://doi.org/10.5517/ccdc.csd.cc2mcj1l); (c) CCDC 2422100, Experimental Crystal Structure Determination, 2025, DOI: [10.5517/ccdc.csd.cc2m9d8m](https://doi.org/10.5517/ccdc.csd.cc2m9d8m).

